Eulerian and Lagrangian transport by shallow-water breaking waves EP

ⓘD **Zhihua Xie** (谢志华) **and** ⓘD **Pengzhi Lin** (林鹏智)

COLLECTIONS

EP This paper was selected as an Editor's Pick

View Online   Export Citation   CrossMark

ARTICLES YOU MAY BE INTERESTED IN

A consistent mass–momentum flux computation method for the simulation of plunging jet
Physics of Fluids **34**, 032114 (2022); https://doi.org/10.1063/5.0084894

Deformation and acceleration of water droplet in continuous airflow
Physics of Fluids **34**, 033313 (2022); https://doi.org/10.1063/5.0085210

Effect of the odd and even number of blades on the hydrodynamic performance of a pre-swirl
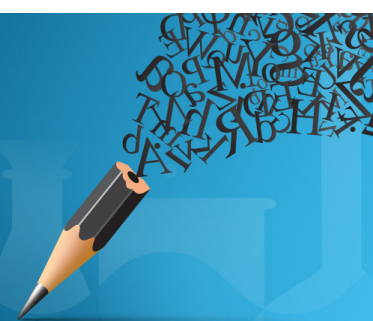pumpjet propulsor
Physics of Fluids **34**, 035120 (2022); https://doi.org/10.1063/5.0080661

Eulerian and Lagrangian transport by shallow-water breaking waves (EP)

View Online　　Export Citation　　CrossMark

Zhihua Xie (谢志华),[1] (iD) and Pengzhi Lin (林鹏智)[2,a] (iD)

AFFILIATIONS

[1]Hydro-Environmental Research Centre, School of Engineering, Cardiff University, Cardiff CF24 3AA, United Kingdom
[2]State Key Laboratory of Hydraulics and Mountain River Engineering, Sichuan University, Chengdu 610065, China

[a]Author to whom correspondence should be addressed: cvelinpz@scu.edu.cn

ABSTRACT

This study examines the mass and Lagrangian transport, kinematic and dynamic characteristics of shallow-water breaking waves, focusing on the wave breaking, and jet impingement processes. A multiphase Navier–Stokes flow model has been developed to track the origin and trajectory for the jet and the splash-up using both a geometric piece-wise linear interface calculation volume-of-fluid (PLIC-VOF) and the Lagrangian particle tracking approaches. The model is first validated both quantitatively and qualitatively against the experimental data for the plunging jet and the splash-up during wave breaking, in which a good agreement is obtained. The mass transport and the origin of the jet and splash-up are studied using the new multi-component PLIC-VOF approach, and the different regions in the interior of the wave are tracked in an Eulerian way. Both horizontal and vertical drifts for the interior and surface particles are shown using the Lagrangian particles. The location and origin of the plunging jet can be clearly seen from the simulations. Various wave steepness and beach slopes have been investigated for different types of breakers. Furthermore, the detailed jet impingement, velocity, pressure, vorticity, and turbulence fields during wave breaking are discussed and presented, providing more detailed flow fields to gain further insight into the plunging jet and splash-up in shallow-water breaking waves.

I. INTRODUCTION

Eulerian mass and Lagrangian particle transport under breaking waves play an important role in air–sea interaction and material transport in the nearshore zone. Better understanding of shallow-water breaking wave-induced flow phenomena can lead to a better prediction of the ecosystem, water quality, and microplastic transport in coastal waters. Although great efforts have been achieved in the past[1,2] to study the dynamics of breaking waves, detailed studies focusing on the wave breaking and post-breaking processes, together with associated mass and particle transport,[3] are still limited. The complexity of this frequently turbulent, multiphase flow phenomenon during wave breaking and air entrainment processes are still poorly understood.[4,5]

Many laboratory measurements have been carried out to study breaking wave mechanics in deep and shallow water.[6–13] Based on the observation and hypothesis, the detailed mechanism for the plunging jet and the splash-up have been discussed for deep-water[14] and shallow-water[15] breaking waves. Clearly, more research into the complex wave post-breaking process is required to fully understand the plunging jet impact mechanism.

With the advances in computational fluid dynamics,[16] a number of numerical studies have elucidated the wave breaking mechanism for periodic deep-water breaking waves,[17–23] surf zone breaking waves,[24–32] focusing wave,[33,34] shallow-water breaking waves over complex topography,[35,36] and wave–structure interaction.[37–39] A key requirement for simulating breaking waves is the tracking or capturing of the interface.[40] Numerous methods have been proposed and used to simulate free-surface including wave breaking flows, such as marker-and-cell,[41] volume-of-fluid (VOF),[42] level set,[43] front-tracking,[44] phase field,[45] and meshless (particle)[28,46] methods. Most of the previous studies for shallow-water breaking waves are validated against experimental measurements in terms of the mean flow and turbulence structures, and a few studies have investigated the detailed wave breaking process. Recently, the development of the detailed plunging jet and air entrainment has been investigated for periodic deep-water breaking waves using the large-eddy simulation[20,23] and direct numerical simulation[21,22] approaches. However, those simulations are initialized with a Stokes wave in a periodic domain, and no quantitative or qualitative comparison against experimental measurements has been made for the geometry of the plunging jet and jet impingement process.

In addition to the wave breaking process, there are also researches to understand the wave breaking onset in both controlled laboratory and numerical wave tanks. Perlin et al.[2] reviewed the progress on the prediction of wave breaking onset in intermediate and deep water, which included the geometric, kinematic, and dynamic criteria. Derakhti and Kirby[34] investigated the breaking onset for unsteady focused wave packets. Recently, Barthelemy et al.[47] proposed a new breaking criterion based on the local energy flux velocity through their potential flow model for gravity waves in intermediate and deep water. Derakhti et al.[48] and Varing et al.[49] also investigated the breaking criterion for shallow-water breaking waves.

During the post-breaking process for shallow-water breaking waves, both laboratory and numerical research have been carried out to study the detailed wave overturning and splash-up. Li[50] carried out experiments to study the splash-up of breaking solitary waves on a sloping beach, in which the profiles for the plunging jet during wave breaking were presented. Several models, such as the potential flow model,[51,52] hybrid model,[53] single-phase particle method,[54] and two-phase volume-of-fluid models,[55,56] have been developed to study the wave overturning process, with good agreement with the experimentally measured wave surface profiles. However, the kinematics and dynamics of the plunging jet and the splash-up are still not well understood due to the complex two-phase flow. Moreover, the mass and Lagrangian transport in shallow-water breaking waves have rarely been investigated, although it has been studied numerically in deep water[57] and non-breaking water waves.[58]

The aim of this study is, therefore, to investigate the mass and Lagrangian transport under plunging jet and the splash-up in shallow-water breaking waves, focusing on the wave pre- and post-breaking processes. In this study, a refined multiphase flow model has been further developed to track the origin and trajectory for the jet and the splash-up using a multi-component approach. In addition, Lagrangian particles are tracked within the water wave to elucidate the particle displacement and their drift in the breaking region. The model is justified by the detailed quantitative and qualitative comparison with the experimental measurement.[50] Several wave heights and slope angles are considered. Furthermore, the detailed jet impingement, velocity, pressure, vorticity, and turbulence fields during wave breaking are discussed and presented, providing detailed flow fields to gain further insight into the plunging jet, splash-up, and associated Lagrangian transport under breaking waves.

The rest of the paper is organized as follows. In Sec. II, we review the mathematical model and numerical method and introduce the computational setup and validation. In Sec. III, we present the observation for the mass transport, Lagrangian particle trajectories, and kinematic and dynamic analysis of the wave overturning and post-breaking processes. Finally, discussion and conclusions are presented in Sec. IV.

II. NUMERICAL MODEL AND SETUP
A. Mathematical model

The mathematical model is based on the Navier–Stokes equations for incompressible flow,

$$\nabla \cdot \boldsymbol{u} = 0, \tag{1}$$

$$\frac{\partial(\rho \boldsymbol{u})}{\partial t} + \nabla \cdot (\rho \boldsymbol{u} \otimes \boldsymbol{u}) = -\nabla p + \nabla \cdot \left[(\mu + \mu_t)(\nabla \boldsymbol{u} + \nabla^{\mathrm{T}} \boldsymbol{u})\right]$$
$$+ \rho \boldsymbol{g} + \sigma \kappa \tilde{\mathbf{n}} \delta, \tag{2}$$

where t is the time, p represents pressure, $\boldsymbol{u}$ is the velocity vector, $\boldsymbol{g}$ the gravitational acceleration vector, and ρ and μ are the density and dynamic viscosity of the fluid, respectively. The surface tension is considered by the continuum surface force method, with the surface tension coefficient σ, the curvature κ, the interface unit normal $\tilde{\mathbf{n}}$, and the Dirac delta function δ. The turbulent eddy viscosity $\mu_t = \rho C_\mu k^2/\varepsilon$ is calculated from the $k-\varepsilon$ turbulence model,[59] in which k and ε are the turbulent kinetic energy and turbulent eddy dissipation, respectively, as

$$\frac{\partial(\rho k)}{\partial t} + \nabla \cdot (\rho \boldsymbol{u} k) = \nabla \cdot \left[\left(\mu + \frac{\mu_t}{\sigma_k}\right)\nabla k\right] + P_k - \rho \varepsilon, \tag{3}$$

$$\frac{\partial(\rho \varepsilon)}{\partial t} + \nabla \cdot (\rho \boldsymbol{u} \varepsilon) = \nabla \cdot \left[\left(\mu + \frac{\mu_t}{\sigma_\varepsilon}\right)\nabla \varepsilon\right] + C_{1\varepsilon}\frac{\varepsilon}{k}P_k - C_{2\varepsilon}\rho\frac{\varepsilon^2}{k}, \tag{4}$$

in which C_μ, σ_k, σ_ε, $C_{1\varepsilon}$, and $C_{2\varepsilon}$ are the empirical coefficients,[59] and $P_k = \mu_t(\partial u_i/\partial x_j + \partial u_j/\partial x_i)^2/2$ represents the turbulent production term.

The constitutive relations for the density and dynamic viscosity of the fluid in the momentum equation are calculated by

$$\rho = F\rho_{\mathrm{w}} + (1 - F)\rho_{\mathrm{a}}, \tag{5}$$
$$\mu = F\mu_{\mathrm{w}} + (1 - F)\mu_{\mathrm{a}}, \tag{6}$$

where F is the volume fraction of water, and the subscripts a and w represent air and water, respectively. The movement of the air–water interface is solved by the volume fraction equation as

$$\frac{\mathrm{d}F}{\mathrm{d}t} = \frac{\partial F}{\partial t} + \boldsymbol{u} \cdot \nabla F = 0. \tag{7}$$

A multi-component approach is developed to study the mass transport for water waves as

$$\sum_{i=1}^{N_c} \alpha_i = F, \tag{8}$$

where α_i is the volume fraction for component i and N_c is the number of components in the water wave. The movement of each component is governed by the volume fraction advection equation as above.

A Lagrangian particle tracking method is used to study the water particles within the water waves and their locations can be tracked as

$$\frac{\mathrm{d}\boldsymbol{x}_p}{\mathrm{d}t} = \boldsymbol{u}_p, \tag{9}$$

where $\boldsymbol{x}_p$ and $\boldsymbol{u}_p$ are the location and velocity of the Lagrangian particle, respectively.

B. Numerical method

A Cartesian grid multiphase flow solver (Xdolphin3D), based on the 2D Reynolds-averaged Navier–Stokes (RANS)[56] or the 3D large-eddy simulation (LES)[35] approaches, is used for the computations. The finite volume method is used to discretize the governing equations on a staggered Cartesian grid. The central difference scheme is used to calculate the gradients in the pressure and diffusion terms. A high-resolution scheme,[56] which combines high-order accuracy with monotonicity, is used for the advection terms. A Cartesian cut-cell method[60] is developed to deal with the sloping beach. The SIMPLE algorithm is
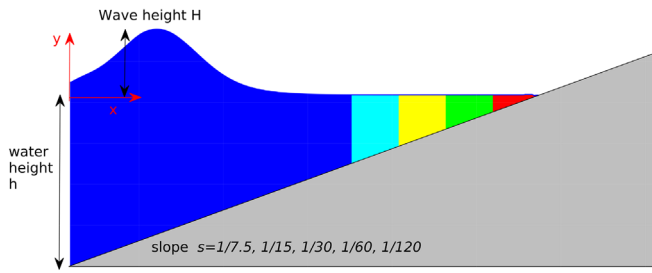
FIG. 1. Sketch of a solitary wave breaking on a sloping beach (not scaled). Additional four nearshore regions with a width of $0.1h/s$ each (red, green, yellow, and cyan) are also captured by the geometric PLIC-VOF method.

FIG. 2. Convergence study for three different meshes for $H/h = 0.3$ over a slope $s = 1 : 15$ during wave breaking at $t' * \sqrt{g/h} = 11.86$, where t' starts when the wave enters the toe of the beach as defined in the experiment.[50]

employed for the pressure-velocity coupling in this study with a second-order backward Euler method for the time stepping. The multiphase flow code Xdolphin3D has already been extensively verified and validated through numerous examples for wave breaking flows,[30,35,36,56] dam-break flows,[61] wave-structure interaction,[39] LES studies of free surface flows over rough beds[62] and with moving bodies.[60] Compared to our previous studies, in which an algebraic VOF method CICSAM[63] was implemented for interface capturing, in this study, the Xdolphin3D code has been further refined to capture the air–water interface using a geometric PLIC-VOF (piece-wise linear interface calculation volume-of-fluid) method,[64] and the balanced-force continuum surface force model[65] is implemented for the surface tension effect. A multi-component approach[66] is developed, based on the PLIC-VOF method, to capture the mass transport of different regions of the breaking waves. In addition, the Lagrangian particle tracking algorithm is implemented in the model to track the interior and surface particles of water waves, in which the particle velocities are interpolated using the bilinear interpolation from the Cartesian grid velocities.

C. Computational setup

The numerical model was setup to replicate breaking waves in the laboratory experiments,[50] in which detailed measurements of plunging jet and the splash-up in a wave flume were collected. As the breaking waves observed in the experiment are mostly 2D before the jet impingement and become 3D at the later stage of the splash-up, which is beyond the scope of the present study, 2D RANS simulations are carried out in this parametric study with finer mesh in the breaking region. In addition, this would also allow a detailed investigation of the geometric properties during wave breaking. Figure 1 shows the sketch of a solitary wave over a sloping beach, in which h is the still water depth and H is the solitary wave height. x and y are the horizontal and vertical coordinates, respectively, and the still water level above the toe
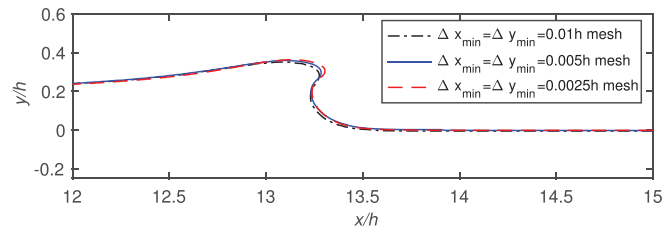
of the beach is used as the origin of the coordinate system. The slope of the beach is s and the still water depth is $h = 0.3048$ m. The size of the computational domain is $1.25h/s \times 1.75h$ and a non-uniform grid is used in the simulation with minimum meshes located near the breaking region. The solitary wave is generated at the inlet by specifying the water surface elevation and the water particle velocities, which can be obtained from the analytical solution for solitary waves.[67] Zero-gradient boundary conditions are used at the outlet and the top of the numerical domain, whereas for the sloping beach, the wall function for the $k - \varepsilon$ turbulence model is applied. The time step is adapted so that the Courant–Friedrichs–Lewy number is smaller than 0.2.

Both Eulerian and Lagrangian approaches are used to track the water waves during wave breaking. Additional four regions with a width of $0.1h/s$ each near the shoreline are captured by the PLIC-VOF method, where the geometry of the interface is explicitly reconstructed and advected in a Lagrangian way. In addition, Lagrangian particles are also seeded in the flow with the same mesh resolution in those regions. So that the origin and the trajectory of the plunging jet and subsequent splash-up can be determined. Various cases for a different incident solitary wave steepness (H/h) and the effect of the slope s are considered. The physical and computational parameters are shown in Table I.

D. Validation

Additional convergence tests (shown in Fig. 2) have been carried out in three different non-uniform grids ($60/s \times 70$, $120/s \times 140$, $240/s \times 280$) with minimum meshes ($\Delta x = \Delta y = 0.01h, 0.005h, 0.0025h$) to check the level of refinement to predict the wave profile during wave overturning. It is found that for $s = 1 : 15$, there is only a slight change on the tip of the overturning wave between the medium (1800×140) and fine (3600×280) meshes; thus, the $120/s \times 140$ non-uniform grid with minimum meshes $\Delta x = \Delta y = 0.005h$ is selected in the simulations thereafter.

The computational results for $H/h = 0.3$ before the impingement and $H/h = 0.4$ during the splash-up for $s = 1 : 15$ are shown

TABLE I. Physical and computational parameters used in the numerical simulations.

Slope s	Depth h (m)	H/h	Wave celerity C	$Re_w \left(\frac{\rho_w Ch}{\mu_w} \right)$
$\frac{1}{7.5}, \frac{1}{15}, \frac{1}{30}, \frac{1}{60}, \frac{1}{120}$	0.3048	$0.1 - 0.4$	$\sqrt{g(h+H)}$	$6.2–7.0 \times 10^5$
$\rho_w (\mathrm{kg \cdot m^{-3}})$	$\rho_a (\mathrm{kg \cdot m^{-3}})$	$\mu_w (\mathrm{kg \cdot m^{-1} \cdot s^{-1}})$	$\mu_a (\mathrm{kg \cdot m^{-1} \cdot s^{-1}})$	$\sigma (\mathrm{N \cdot m^{-1}})$
998.0	1.185	8.89×10^{-4}	1.83×10^{-5}	0.072

in Fig. 3 and compared with the experimental measurements.[50] Figure 3(a) shows a quantitative comparison between the predicted results and the experimental data for $H/h = 0.3$. It can be seen that when the wave travels along the slope, the wave height increases due to the wave shoaling effect and with the maximum wave height being obtained just before the wave front becomes vertical. A plunging jet is developed during the wave overturning process with an air cavity enclosed beneath the jet. Although the experimental data are only available just before the jet impingement, the shape of the overturning jet and the breaking location is well captured by the present multiphase model.

The wave breaking and post-breaking process obtained by the numerical simulation for $H/h = 0.4$ are superimposed on the

laboratory photographs[50] in Fig. 3(b). It can be seen that a plunging jet is formed during the wave breaking process. The overturning jet length becomes longer and eventually impinges on the undisturbed water surface ahead to initiate the splash-up process with an air cavity being enclosed beneath the plunging jet. At this stage, pushed by the primary jet, a secondary jet is generated to move upward onshore and some parts of the water move backward offshore which forms a rough water surface in the cavity. During the splash-up process, the height of the secondary jet increases, and spray and droplets can be observed from the jet. In the end, the cavity collapses, and a third jet is formed on the back face of the secondary jet and will eventually curl back toward the incident wave due to the gravity effect.[50] Figure 3 shows that a good
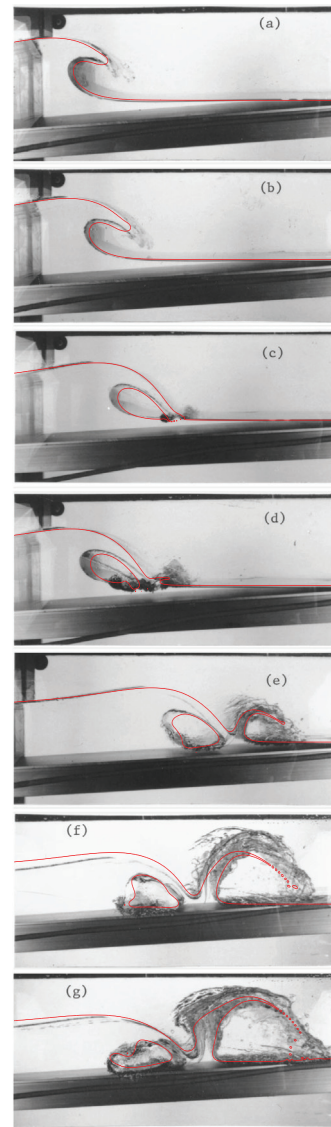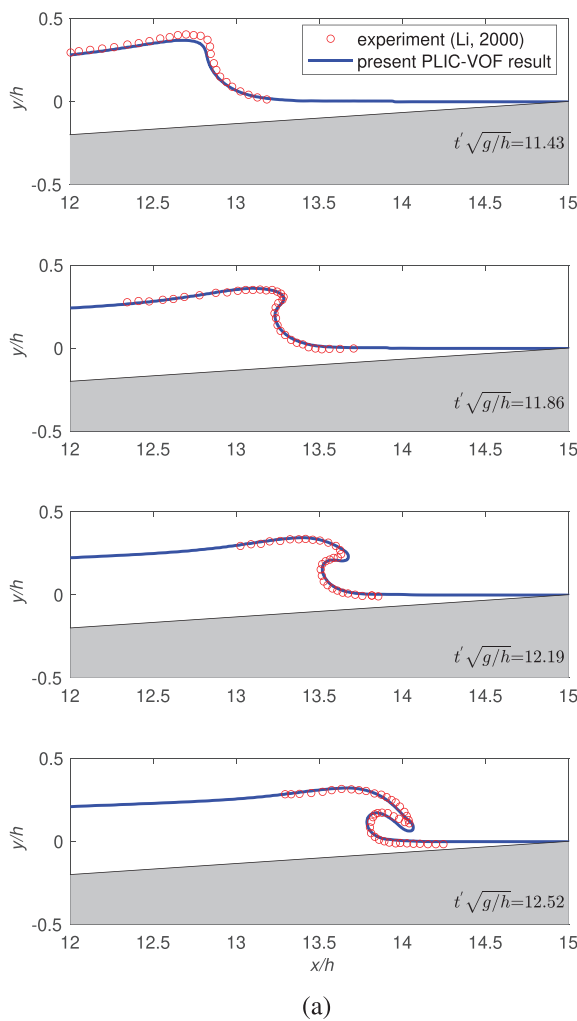

FIG. 3. Quantitative (a) and qualitative (b) comparison with the experimental measurement[50] for a solitary wave over a $s = 1:15$ sloping beach for $H/h = 0.3$ (a) and 0.4 (b).

agreement is obtained between the numerical and experimental results. There is a slight discrepancy in the development of the aerated region and the height of the complex splash-up, which is attributed to the 3D air entrainment and turbulence generation, which is beyond the scope of the present study. Overall, the wave breaking process is well reproduced by the present model, including the wave overturning process, plunging jet impinging angle, and subsequent splash-up process. The small droplets are also captured due to the PLIC-VOF method, which is better than the previous 2D results in the literature (e.g., Refs. 54 and 56).

III. RESULTS

A. Mass transport and the origin of the plunging jet and splash-up

It is worth noting that although there is much research for breaking waves, the detailed study of the overturning process and the splash-up in shallow water are still very limited. The mass transport of the interior fluid of the wave is investigated in this section, which provides insight into the origin and onset for the plunging jet and splash-up.

1. Mass transport

Stokes[68] showed that the interior of the fluid in a progressive, irrotational wave does not have a closed trajectory path; instead, they have a mean mass transport referred to as Stokes drift. Longuet–Higgins[69] investigated the effect of the viscosity in long-time mass transport and highlighted that the observations of mass transport in the interior of the deep-water water waves are similar to the Stokes drift; however, the observations appear to be uncertain in shallow water. Due to the difficulty in the laboratory to measure the mass transport, Deike et al.[57] studied the Lagrangian transport of breaking deep-water focusing waves by tracking tracer particles. Here, the mass transport in shallow-water breaking waves is investigated by the Eulerian tracking of four regions with a width of $0.1h/s$ each near the shoreline, which is similar to put four different dyes into the water in a laboratory wave tank.

Figure 4 shows the mass transport traced by the PLIC-VOF method for four different incident waves ($H/h = 0.1 - 0.4$) over a $s = 1 : 15$ sloping beach. Five different regions [blue: $(0 - 0.6)h/s$; cyan: $(0.6 - 0.7)h/s$; yellow: $(0.7 - 0.8)h/s$; green: $(0.8 - 0.9)h/s$; red: $(0.9 - 1)h/s$] are marked with different colors in which the propagation and evolution of the solitary wave can be clearly seen. It can be seen that the wave breaks further onshore when the incident wave steepness decreases. A similar type of plunging breakers is observed for $H/h = 0.2, 0.3, 0.4$ whereas the collapsing breaker is observed for $H/h = 0.1$. It can be seen from Fig. 4 that the water near shore (red and some part of the green region) are nearly stationary before the wave approaches. When the wave comes onshore, the water particles start to move and the surface drift is larger than the bottom drift. In the offshore region for $H/h = 0.4$, some fingering structures can be seen between the blue and cyan region due to the particle trajectories in the interior of the fluid of the solitary wave, with some offshore region (blue) penetrating into the neighboring region (cyan) in the vicinity of the upper layer of the wave.

#### 2. Development of the plunging jet

The wave becomes steep due to the shoaling effect and the front face of the wave becomes nearly vertical as the wave breaking process starts. At this stage, a plunging jet is formed with the tip originating from the vertical face. For $H/h = 0.4$, it can be seen that the front face becomes vertical near the boundary between the yellow and green regions. A similar phenomenon can be found for $H/h = 0.2$, which is between the green and red regions. For $H/h = 0.3$, the front face becomes vertical in the middle of the green region. As the initial state of all these regions is known, the origin of the plunging jet can be roughly estimated as $0.8h/s, 0.85h/s, 0.9h/s$ for $H/h = 0.4, 0.3, 0.2$, respectively. As the lowest wave steepness case $H/h = 0.1$, the plunging jet is developed with a single color region, but we can roughly estimate the origin of the jet is close to the shoreline and then formed a collapsing breaker. During wave overturning, it can be seen from Fig. 4 that the water surface ahead of the origin of the jet also follows the same trend during wave curling, and a plunging jet is developed comprising of an onshore region in the upper part and nearshore region in the lower part of the jet. At this stage, an air cavity is entrapped under the plunging jet and closed until the jet impingement.

3. Development of the splash-up

During wave breaking, the overturning jet touches down the undisturbed water surface ahead and a splash-up is generated. Many researchers have investigated the detailed splash-up process (see review[4]) both experimentally[14] and numerically[20] for deep-water breaking waves. Peregrine[1] analyzed the wave overturning and splash-up process in detail for breaking waves on beaches, and Watanabe et al.[26] studied the velocity field to better understand the splash-up in the surf zone. However, very little work has been contributed to the mass transport after the jet touchdown and to elucidate the origin of the splash-up process. This is even more difficult in laboratory studies due to the complex multiphase flows and transport induced by the breaking wave.

It is worth noting that the case $H/h = 0.4$ has been qualitatively compared with the experimental measurements for the splash-up process in Fig. 3(b), which validates the model for predicting the impingement point and post-breaking process. During the splash-up process for $H/h = 0.4$ shown in Fig. 4(a), the plunging jet impinges the undisturbed water surface ahead (red region), and splits into two parts: the front part of the jet (yellow region) moves upward with an angle to generate a secondary jet, which is comprised of the primary jet on the upper face and the undisturbed surface on the lower face; the rear part of the jet (yellow and green regions) moves backward against the flow, creating a rough surface and circulation along the cavity. Two strong counter-rotating vortices can be observed during the splash-up process. At a later stage, the re-circulation part (green region) starts to move upward with the secondary jet, and small droplets are detached from the tip of the secondary jet when it becomes too thin.

For the case $H/h = 0.3$ and $H/h = 0.2$ shown in Figs. 4(b) and 4(c), similar splash-up process can be observed whereas the plunging jet is formed purely from the green region for $H/h = 0.3$. It can be seen that the upper part of the plunging jet pushes the undisturbed surface ahead to generate the secondary jet, and the lower part reverts back toward the cavity. When the wave steepness H/h decreases, the
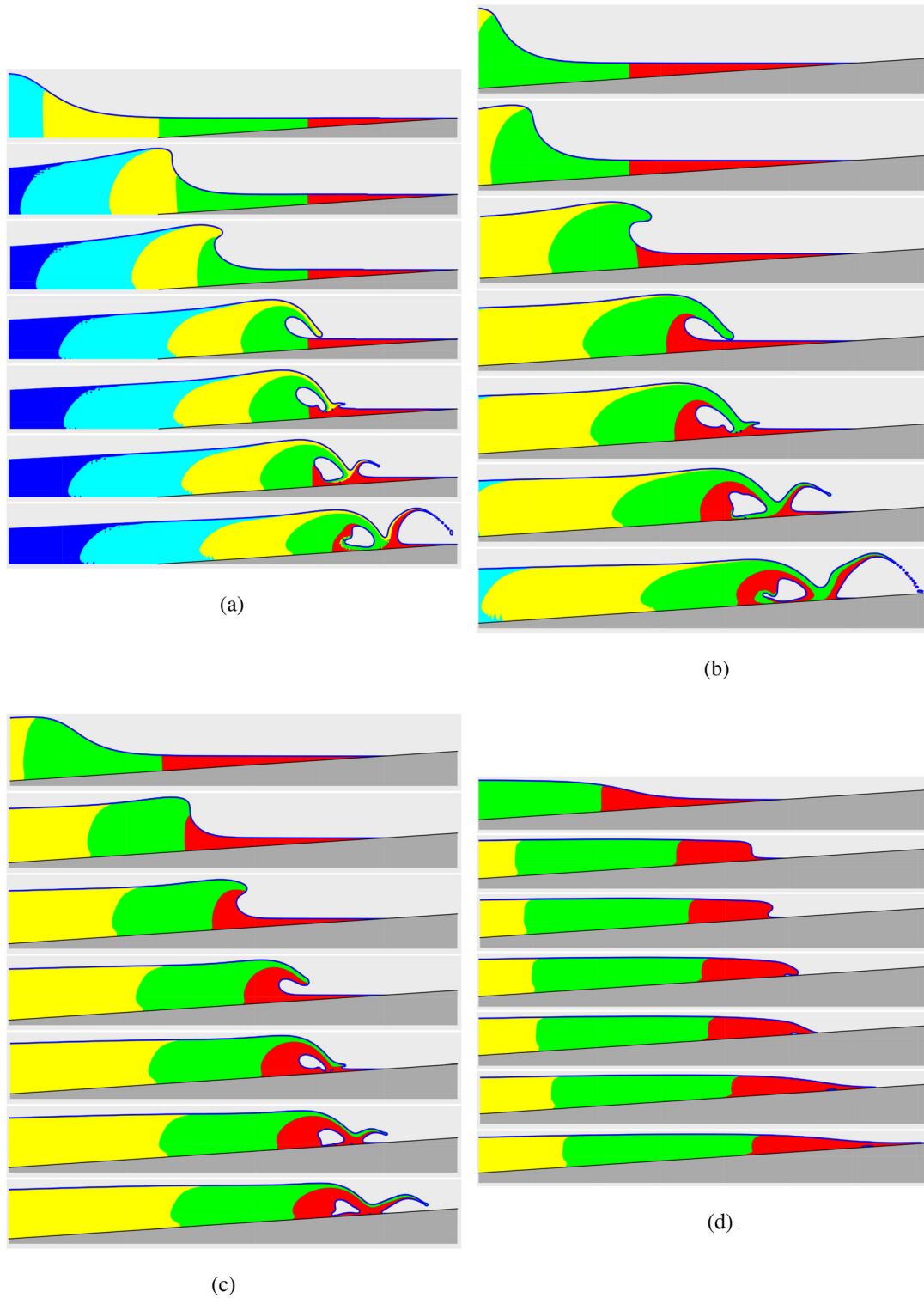
FIG. 4. Mass transport for various incident waves with $H/h = 0.4$ (a), 0.3 (b), 0.2 (c), and 0.1 (d) along a $s = 1:15$ sloping beach. Five different regions [blue: $0 - 0.6h/s$; cyan: $(0.6 - 0.7)h/s$; yellow: $(0.7 - 0.8)h/s$; green: $(0.8 - 0.9)h/s$; and red: $(0.9 - 1)h/s$] are marked with different colors at $t = 0$.
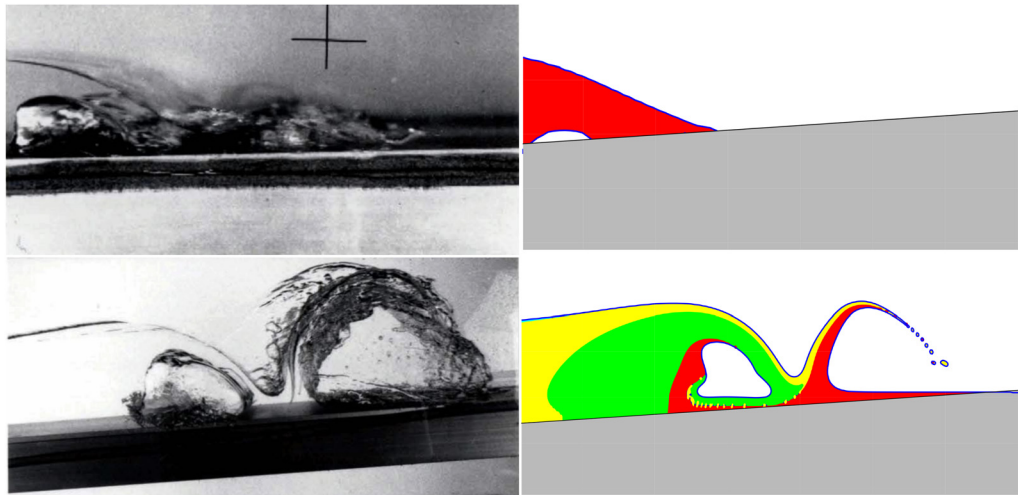
FIG. 5. Development and origin of the splash-up over a $s = 1 : 15$ sloping beach. Top is without a splash-up for $H/h = 0.1$ and below is with a splash-up for $H/h = 0.4$. Left panel is the experimental photos obtained in Li.[50]

wave breaks further onshore at a lower water depth; thus, the height and the inclined angle of the splash-up decreases.

It is worth mentioning that when the wave steepness decreases further at $H/h = 0.1$, the impingement point is already past the shoreline, and thus only collapsing breaker is observed without any splash-up, which is also consistent with the experimental measurements shown in Fig. 5.

B. Lagrangian displacement of particles

After discussing the mass transport in the Eulerian framework, we present the Lagrangian displacements of particles for shallow-water breaking waves in this section. The displacement of water particles can be expressed as

$$x(t) = x_0 + \int_{t_0}^{t} u(x(\tau), y(\tau), \tau) d\tau, \qquad (10)$$

$$y(t) = y_0 + \int_{t_0}^{t} v(x(\tau), y(\tau), \tau) d\tau, \qquad (11)$$

where x_0 and y_0 are particles' initial location at time t_0. The drift in the horizontal and vertical directions are defined as $drift_x = x(t) - x_0$ and $drift_y = y(t) - y_0$, respectively.

We select the example for the breaking wave case $H/h = 0.4$ and $s = 1 : 15$ to show here, which is the strongest plunging breaker considered in the present study.

1. Particle trajectories

Figure 6 shows an example of the particle trajectories for the shallow-water breaking wave for $H/h = 0.4$ and $s = 1 : 15$, which corresponds to the middle of the mass transport regions shown in Fig. 4(a). In shallow-water waves, the water particle trajectories follow transitional water elliptical orbits with higher velocity near the wave surface.[67] However, for solitary waves, it can be seen from Fig. 6(a) for the cyan region that there is no backward motion along with the wave

propagation and there is drift horizontally and vertical excursion decreases with the depth below the water surface. These would be the typical particle motions along the beach which is not involved with wave breaking.

For the yellow region shown in Fig. 4(a), it can be clearly seen from Fig. 6(b) that the particle motions near the water surface are totally different although the particles with deeper water depth follow a similar trend in Fig. 6(a). As the upper part of the plunging jet is formed from the yellow region, the particle trajectories near the water surface demonstrate the jet touchdown, re-bouncing after the first and secondary splash-up. The particles have much larger horizontal and vertical drift when they propagate along the breaking point.
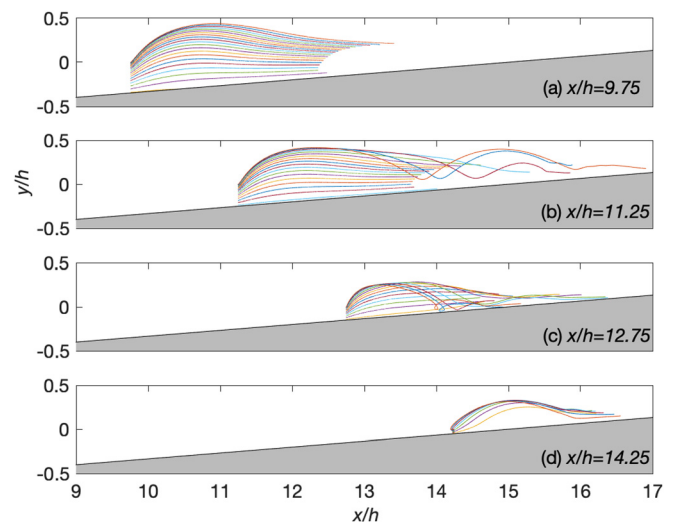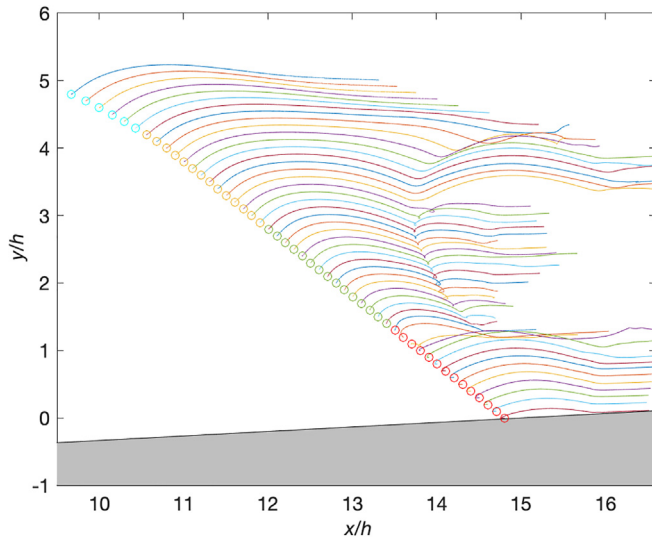

FIG. 6. Trajectories of the particles initially along a vertical line at the center of the four tracked regions: (a) cyan, (b) yellow, (c) green, and (d) red from $x/h = 9 - 15$ shown in Fig. 1. This case shown here is for $H/h = 0.4$ and $s = 1/15$.

FIG. 7. Trajectories of the particles initially at the air–water interface for $H/h = 0.4$ and $s = 1/15$. For the sake of clarity, each particle away from the shoreline is shifted upward in order to see the whole picture. The circles are the initial position of the particles, whereas the colors of the circle correspond to the regions shown in Fig. 1.

Figure 6(c) shows the green region shown in Fig. 4(a). As this region forms the inner part of the plunging jet, a swirl shape motion during jet curling down is observed for the particles near the air–water interface. In addition, a backward motion can be clearly seen during the first splash-up to form the cavity and then propagating along the main wave. The vertical drift is much smaller in this region as they are not included in the secondary jet, which is consistent with the observation shown in Fig. 4(a).

Figure 6(d) shows the particle trajectories near the shoreline for the red region shown in Fig. 4(a). It can be seen that there are fewer particles along the vertical due to the shallow water depth. The particles remain almost stationary before the wave arrives and start to

move when the plunging jet impinges the water surface during the splash-up. The particles closer to the water surface have a higher vertical movement as they form the secondary jet shown in Fig. 4(a). They eventually move along the beach slope when the secondary jet impacts on the bed.

It is worth mentioning that the Lagrangian transport for the breaking solitary waves is different from the deep-water focusing waves studied by Deike et al.[57] The shallow-water breaking waves could have larger horizontal and vertical drift, and the backward motion is only observed for the splash-up to form the air cavity near the breaking point.

2. Surface transport

The displacement of particles at the air–water interface is studied here, which plays an important role in pollutant transport and gas and momentum transfer during air–sea interaction. Figure 7 shows the trajectories of the particles initially at the air–water interface in the four regions shown in Fig. 1, where their initial locations are represented as circles and colored by their region id. For the cyan region (x/h is between 9.0 and 10.5), they have similar displacement and the particles remain almost horizontal when the wave passes by. For the yellow region (x/h is between 10.5 and 12.0), it can be seen that the particles start to move downward after initially rising by the wave, and they gradually have larger horizontal drift and higher vertical variation when moving onshore as they form part of the plunging jet. When they are closed to the green region, both horizontal and vertical drifts are decreased. For the green region (x/h is between 12.0 and 13.5), the re-bouncing with backward motion can be clearly seen, which is different from the re-bouncing with a forward motion for the yellow region. The backward motion is gradually increased and then decreased when moving toward the shoreline. Both horizontal and vertical drifts in the green region are smaller than that in the yellow region offshore. For the red region (x/h is between 13.5 and 15.0), there are two areas separated by the impingement point, which is consistent with the mass transport shown in Fig. 4(a).

(a)

(b)
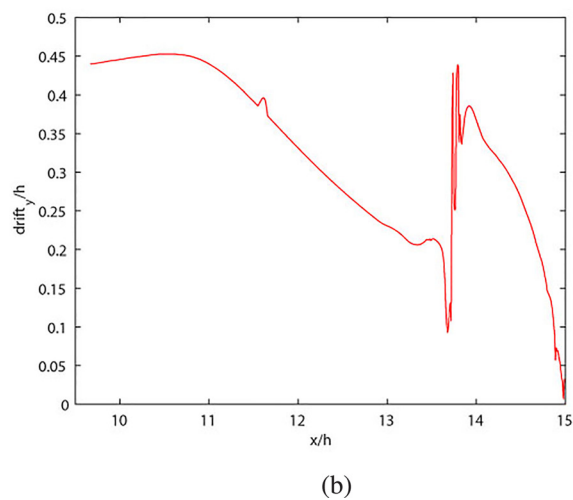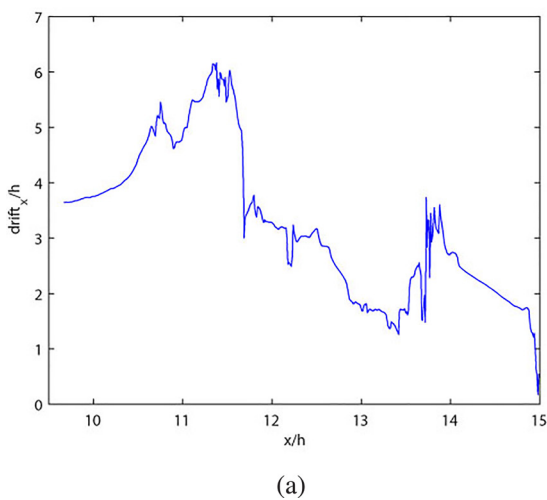
FIG. 8. Total horizontal (a) and vertical (b) drift of the particles initially at the air–water interface as a function as their initial streamwise locations for $H/h = 0.4$ and $s = 1/15$.

In order to compare the total drift of the surface particles during wave breaking (for a time interval of $17\sqrt{h/g}$), we compare the maximum horizontal and vertical drift relative to their initial locations in Fig. 8 as a function of their streamwise locations. The total horizontal drift is gradually increased in the cyan region when moving onshore. The maximum horizontal drift is in the yellow region, with two local maximum values: one forms the top of the main wave after breaking and the another one forms the tip of the plunging jet, which travels furtherest from its initial location. After the original tip of the jet, the total drift is significantly reduced in the horizontal direction. The total horizontal drift in the green region is gradually decreased with the decrease in the water depth. For the red region near the shoreline, it can be seen that the total horizontal drift has the maximum value at the impingement point and gradually decreases toward both ends, with minimum total drift being observed in the vicinity of the shoreline.

For the total vertical drift shown in Fig. 8(b), it is gradually increased during wave shoaling and obtains its maximum value when the wave crest becomes highest during wave breaking. When moving toward the shore, the total vertical drift starts to decrease in the yellow and green regions during wave overturning, and starts to increase suddenly at the impingement point in the red region during the splash-up cycles before decreasing again toward the shoreline. It is worth noting that the water particles near the impingement point can achieve similar heights during splash-up cycles when compared to the maximum water surface height at the onset of breaking.

C. The trajectory and development of plunging jet

In order to study the detailed formation and development of the plunging jet during the wave overturning process, the trajectory and geometric properties of the plunging jet up to the impingement point
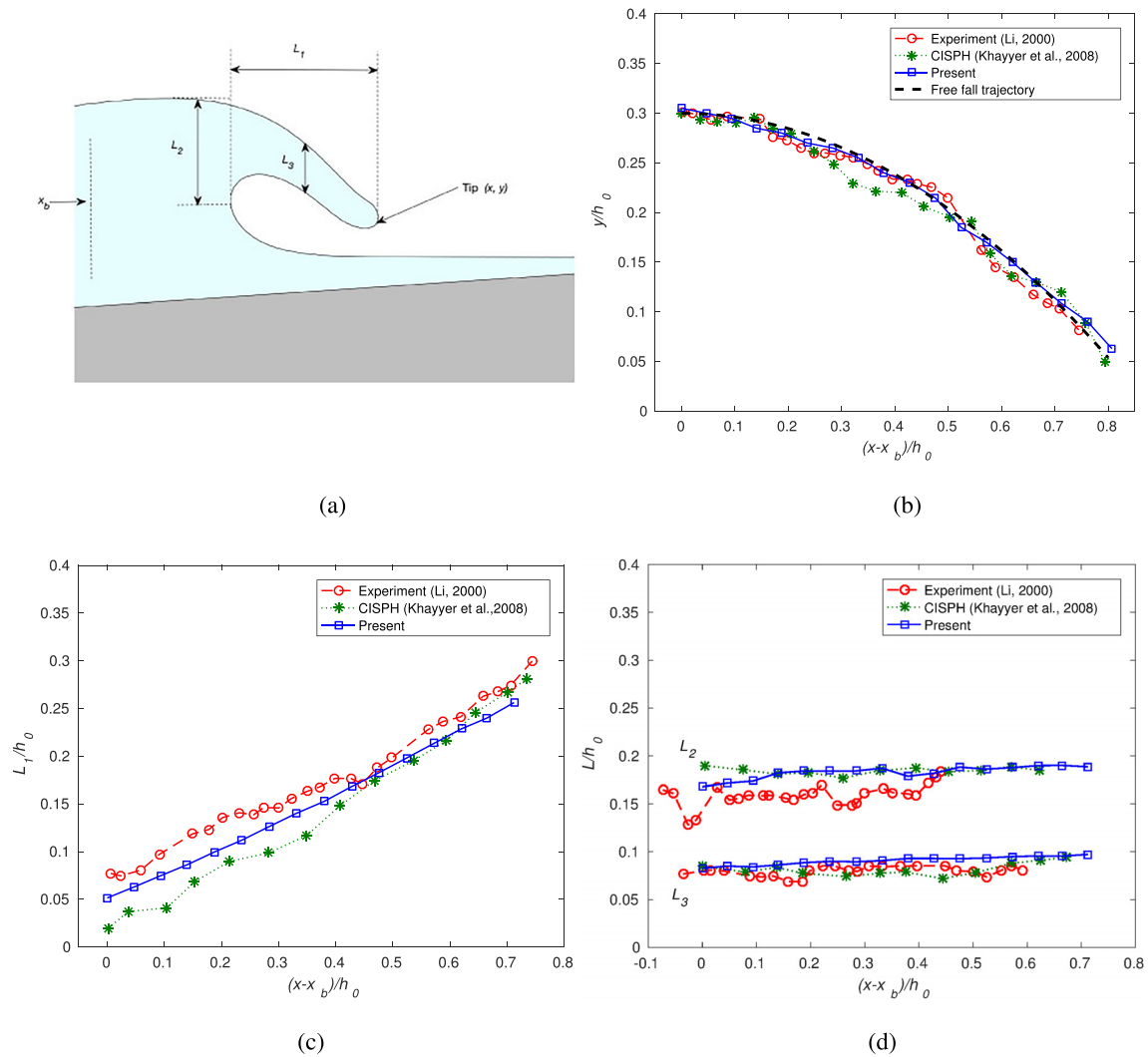

(a)

(b)

(c)

(d)

FIG. 9. Trajectory and the development of the plunging jet during wave overturning: definition sketch of plunging jet (a); jet trajectory (b); the geometric parameters L_1 (c); and L_2 and L_3 (d).

are compared with the experimental data in Li[50] for the case $H/h = 0.3$. In the simulation, the tip of the plunging jet is tracked as a function of the location (x, y) during wave breaking. Three geometric properties are used to represent the shape and development of the plunging jet as shown in Fig. 9(a), in which the length of the jet L_1 is defined as the horizontal distance between the tip of the plunging jet and the front water surface which is nearly vertical. The thickness of the plunging jet is presented by two heights L_2 and L_3. L_2 is the vertical jet thickness at the wave front surface and L_3 is the jet thickness at half of the length, i.e., $L_1/2$. These geometric parameters show the temporal and spatial variations of the jet development, which could be used to inform some simple models to describe the wave overturning process.

1. The trajectory of the plunging jet

Figure 9(b) shows the jet trajectory for the incident wave $H/h = 0.3$ as a function of the jet location with respect to the breaking point x_b, which is defined as the location when the front face of the wave becomes vertical. Both experimental data[50] and the CISPH (corrected incompressible smooth particle hydrodynamics) method[54] are included for comparison. It can be seen that both numerical results by the present study and the CISPH method are similar and both agree well with the experimental measurements.

The free fall trajectory as discussed in Li[50] is also plotted in Fig. 9(b), which is the trajectory of a free-falling object with the initial horizontal velocity assumed to be the wave speed C. It can be observed that there is a good agreement with the free fall trajectory with both experimental and numerical results, indicating that once the plunging jet is ejected from the breaking wave, it behaves like a free-falling jet until it impinges the water surface ahead.

2. The geometric properties of the plunging jet

Figures 9(c) and 9(d) show geometric properties of the plunging jet as a function of the jet location with respect to the breaking point x_b.

It can be seen from Fig. 9(c) that the predicted length of the jet L_1 increases linearly along with the distance during wave overturning, which is consistent with the laboratory observation and the CISPH simulation. The linear slope indicates that the horizontal velocity for the tip of the plunging jet nearly keeps constant once the wave starts to break. There is some discrepancy between the three results, and it is mainly due to the different calculation of the initial length when the wave starts to break.

Figure 9(d) shows the evolution of the jet thickness during wave overturning. It can be seen that the thickness of the jet is nearly constant during wave propagation. The predicted jet thickness L_2 is similar to the result obtained by the CISPH method, with both slightly overestimating the thickness when compared to the experimental data.[50] The predicted jet thickness L_3 at the half length of the jet is approximately half the thickness at the wave front L_2, which is consistent with both the experimental and CISPH results.

3. Velocities and acceleration of the plunging jet just before impingement

Figure 10 shows the velocity and acceleration fields before the plunging jet touches the water surface for the case $H/h = 0.4$ and
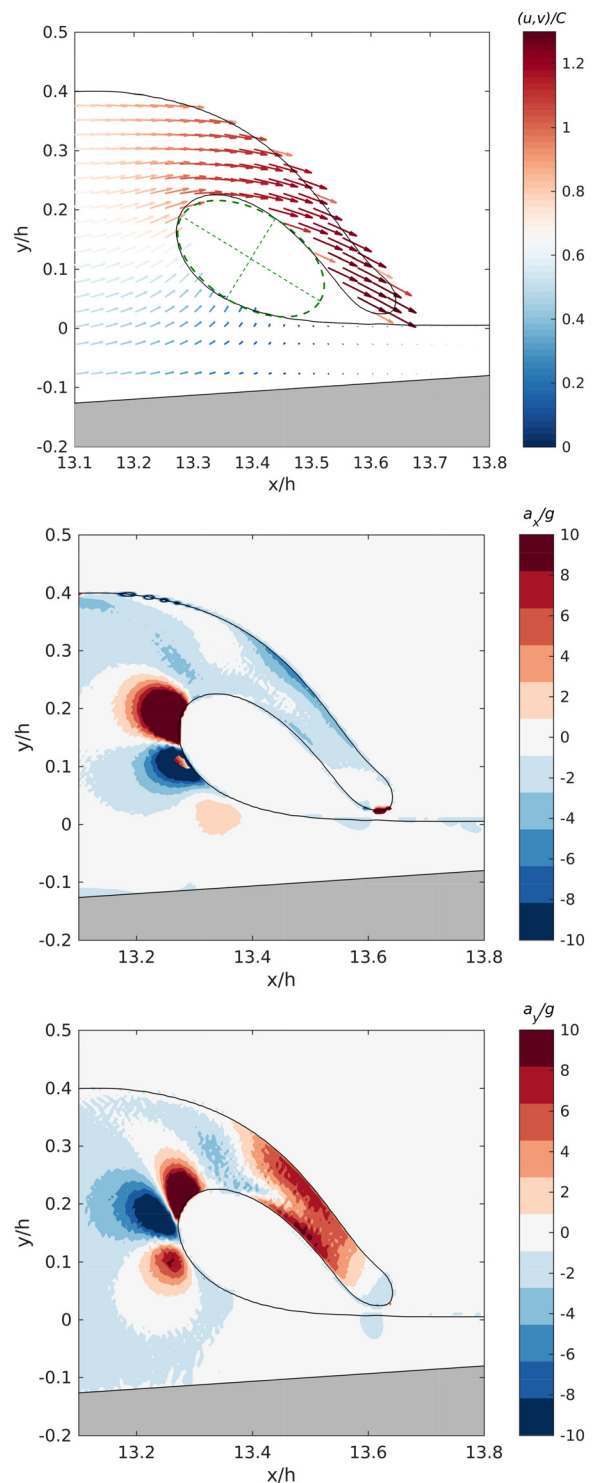
FIG. 10. Velocity vectors (top), horizontal (middle), and vertical (bottom) acceleration components for the plunging jet during wave overturning. For clarity, only every fifth vector is shown here. The fitted $\sqrt{3}$ aspect-ratio ellipse is also shown under the plunging jet with an angle of $-32°$.

$s = 1/15$. The water particle velocity increases from the bottom toward the water surface. The velocity is greater than the wave celerity C when the wave starts to break with the maximum velocity $1.3C$ being located near the tip of the overturning jet. It can be seen that the front face on the incident wave has maximum horizontal acceleration a_x with a positive sign in the upper part and a negative sign in the lower part at the vertical face due to the jet curling down. The horizontal acceleration a_x at the tip is nearly zero, which confirms the assumption for the constant horizontal velocity during wave overturning in Sec. III C 1. For the vertical acceleration a_y, the middle of the front face accelerates downward with both sides upward. The vertical acceleration at the tip of the plunging jet is around $1.2g$ and there is resistance from the cavity beneath the plunging jet during curling down. The observed velocity and acceleration field are consistent with those values of particle image velocimetry measurements of monochromatic waves.[70]

It was noticed in New[71] that a certain region of the wave surface under the plunging jet can be closely approximated by a $\sqrt{3}$ aspect-ratio ellipse, in both shallow and deep water breaking waves. Figure 10 also shows the best fitted $\sqrt{3}$ aspect-ratio ellipse for the enclosed cavity under the overturning jet on the beach. It is shown that the predicted profile also follows New's theory. It is worth noting that the angle of the ellipse is $-32°$ relative to the horizontal direction for the present shallow-water breaking waves, whereas the angle is steeper ($-40°$) in deep-water breaking waves.[17]

D. Kinematics and dynamics during wave breaking

To elucidate the details of internal kinematics and dynamics of breaking waves, three instants (during wave overturning, impingement, and splash-up) are selected to show the horizontal and vertical

velocities, pressure field, vorticity field, and the turbulence intensity field under breaking waves for $H/h = 0.4$, corresponding to the experimental measurements shown in Fig. 3(b). Figure 11 shows the contours of these normalized fields with values presented in the color-bars. During the wave overturning, the plunging jet starts to curl down when $u/C > 1$ and the front face of the incident wave moves upward. The undisturbed water surface remains almost stationary as the magnitude of the velocities is very small. Negative vorticity can be observed at the inner part of the plunging jet as well as some part of the rear water surface and the region near the bottom. Small positive vorticity is generated in the vicinity of the top water surface as there is an air recirculation above. The turbulence intensity is very weak for most parts of the wave and is stronger in the plunging jet. During the plunging jet impingement, the maximum horizontal velocity is approximately $1.5C$ in the tip. In the impact region, some part of the water has the positive vertical velocity to form the secondary jet moving upward and some part of the water has the negative vertical velocity moving toward the bottom, which creates a shear layer to form the rough surface in the cavity as observed in Fig. 3(b). High pressure is also generated in that region which pushes the water outward from the impinging point. The vorticity field is also very complex during the wave touching down. An anti-clockwise vortex is formed at the front of the plunging jet. On the rear face of the plunging jet, two counter-rotating vortices are generated at the intersection point. Higher turbulence intensity is also observed in the lower part of the plunging jet. During the splash-up process, a secondary jet is generated and some droplets are formed with higher velocities. The vertical velocity component is nearly symmetric along a line normal to the slope at the impinging point. The high-pressure region moves toward
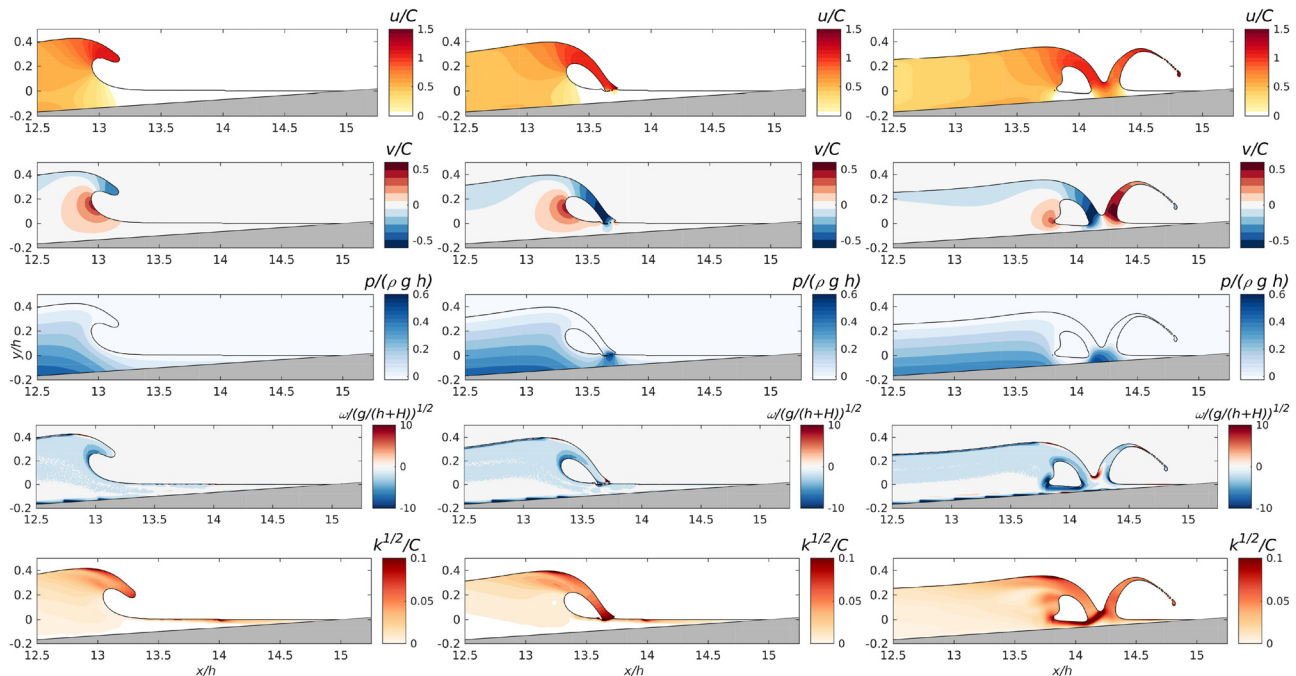

FIG. 11. Detailed normalized streamwise velocity (u), vertical velocity (v), pressure (p), vorticity (ω), and turbulence intensity ($k^{1/2}$) fields during wave overturning (left column), jet impingement (middle column), and splash-up (right column). This is for $H/h = 0.4$ and $s = 1/15$, corresponding to the experimental measurements shown in Fig. 3(b).

the bottom with both positive and negative vorticities generated around the intersecting area, where the turbulence intensity is also high. It is worth mentioning that the splash-up process in shallow-water breaking waves is different from deep-water breaking waves[20] as the splash-up rebounds higher due to the solid boundary effect.

### E. The effect of slope on breaking waves

It is worth noting that not only the incident wave steepness H/h can affect the wave breaking process, the slope s (steep or mild sloping beach) also plays a significant role for shallow-water breaking waves. In this section, the effect of the slope is investigated and the same incident wave steepness $H/h = 0.3$ is kept here in order to make a direct comparison.

In addition to the slope $s = 1/15$ shown in Fig. 4(b), breaking wave results for additional four different slopes $s = 1/7.5, 1/30, 1/60, 1/120$ are shown in Fig. 12. It can be seen that the slope changes the wave breaking process completely even for the same incident wave. For the highest slope ($s = 1/7.5$) shown in Fig. 12(a), the wave starts to break after the shoreline. Even though the jet in the upper surface moves faster initially after the front wave becomes vertical, the lower part of the wave has higher velocity and catches up the front wave without any splash-up being observed.

When the slope decreases for $s = 1/30, 1/60$ in Figs. 12(b) and 12(c), plunging breakers are observed in the simulation, similar to the wave breaking process shown for $s = 1/15$ in Fig. 4(b). However, the detailed wave overturning and splash-up processes are totally different. It is shown that the wave breaks further offshore when the slope decreases, resulting in less vertical thickness $L2$ and $L3$ for the plunging jet. With the decrease in the slope (from 1/15 to 1/60), the water level difference between the rear wave and the undisturbed water surface ahead the jet decreases, and the same trend is also found for the volume of the air cavity enclosed by the plunging jet during wave overturning process.

There is also a significant difference in the splash-up process. For $s = 1/15$, the wave breaks close to the shoreline, and only a single secondary jet is generated during the splash-up process where when the wave breaks further offshore, the secondary jet can also impinge the water surface ahead to generate more than two jets. It is worth noting that even for the same plunging breaking type ($s = 1/30, 1/60$), the subsequent jet-splash cycles are totally different. For $s = 1/30$, the plunging breaker is stronger, and the primary jet catches up with the secondary jet ahead. The front face of the secondary get generates another jet ahead while the rear face is reverted backward toward the primary jet, with complex air entrainment for multiphase flows underneath the main air pocket. For $s = 1/60$, the plunging breaker is much weaker with an angle more inclined to the horizontal. It can be seen that the primary jet cannot catch up with the secondary jet with several jet-splash cycles observed at the front face of the wave. Several smaller air cavities are generated during the splash-up without significant air entrainment in the main body of the wave.

When the slope further decreases for $s = 1/120$ in Fig. 12(d), it can be seen that spilling breaker is observed in the simulation. A much thinner jet is generated during wave overturning and then breaks up into small ligaments or droplets without generating the secondary jet for the splash-up. The wave breaking mainly happens at the front face of the wave, which is different from the plunging breaking waves shown in the present study.
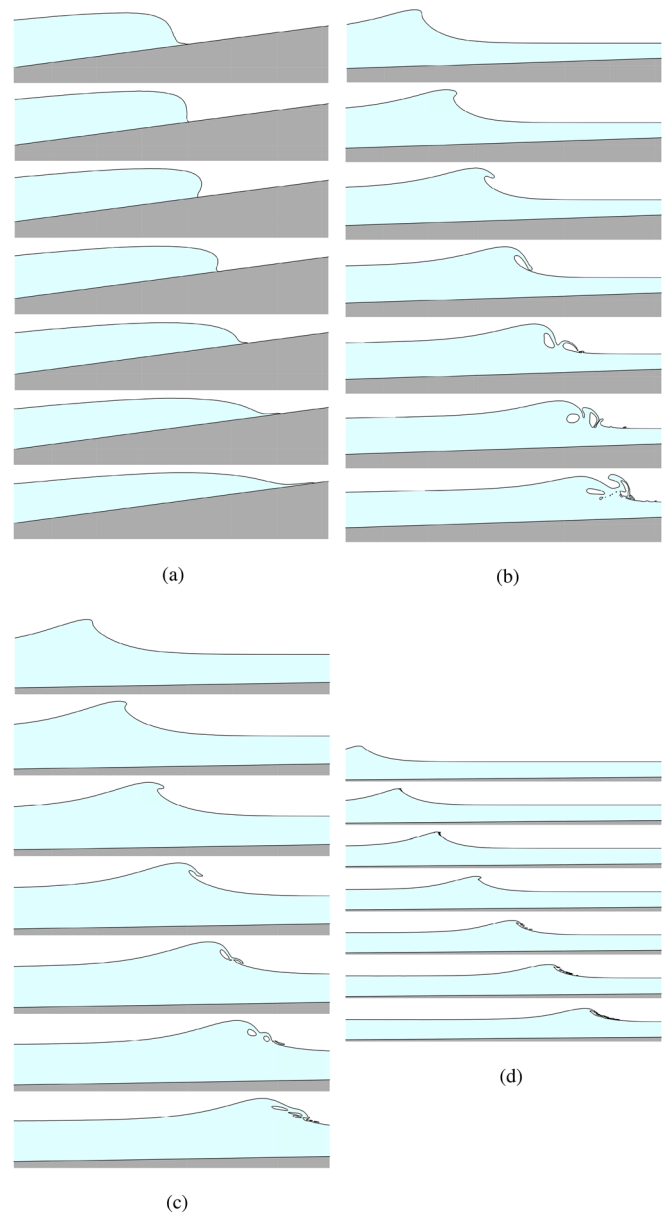
FIG. 12. Breaking wave over different slopes for an incident wave $H/h = 0.3$. Surging breaker $s = 1/7.5$ (a), plunging breakers $s = 1/30$ (b) and $s = 1/60$ (c), and spilling breaker $s = 1/120$ (d) are observed during wave breaking. The time interval between snapshots is $0.2\sqrt{h/g}$ (a), $0.4\sqrt{h/g}$ (b) and (c), and $1.0\sqrt{h/g}$ (d), respectively.

F. Discussion on the wave breaking types

Many researchers have tried to define breaking criteria and breaking characteristics for solitary waves over a slope.[48,49,51] A non-dimensional surf-similarity-type parameter ξ can be used and it is defined for solitary waves as[51]

$$\xi = 1.521 \frac{s}{\sqrt{(H/h)}}. \tag{12}$$

TABLE II. Summary of the numerical results for shallow-water breaking waves with incident wave steepness H/h along the slope s of the shoaling, breaking index, breaking point, surf-similar parameters, breaking type, and splash-up process.

Figure	H/h	s	$\eta_{\max}/H$	$\eta_{\max}/d$	$x_b * s/h$	ξ (12)	Breaking type	Splash-up
Figure 4(a)	0.4	1:15	1.158	2.195	0.79	0.1603	Plunging	One
Figure 4(b)	0.3	1:15	1.225	2.387	0.85	0.1805	Plunging	One
Figure 4(c)	0.2	1:15	1.269	2.643	0.91	0.2267	Plunging	One
Figure 4(d)	0.1	1:15	1.238	1.673	0.98	0.3207	Collapsing	No
Figure 12(a)	0.3	1:7.5	1.055	3.442	0.91	0.3703	Surging	No
Figure 12(b)	0.3	1:30	1.411	1.432	0.70	0.0926	Plunging	Multiple
Figure 12(c)	0.3	1:60	1.491	1.103	0.65	0.0463	Plunging	Multiple
Figure 12(d)	0.3	1:120	1.400	0.950	0.56	0.0231	Spilling	No

This parameter ξ can predict whether the wave will break or not and the type for breaking for a given incident wave steepness H/h along a slope s. From a series of potential flow modeling, Grilli et al.[51] found out that the following values for different breakers as

- Surging breaking: $0.3 < \xi < 0.37$.
- Plunging breaking: $0.025 < \xi < 0.3$.
- Spilling breaking: $\xi < 0.025$.

The simulation results corresponding to the breaking waves presented in the figures of the present study are summarized in Table II. It can be seen that the calculated parameter ξ covers all the ranges considered by Grilli et al.[51] and the obtained breaking types are consistent with their predictions. In addition, a collapsing breaker is identified in the present study, which is in the lower bound of their surging breakers in terms of the value of ξ.

IV. CONCLUSIONS

In this study, a series of 2D numerical simulations have been performed to study the mass and Lagrangian transport of shallow-water breaking waves, focusing on the breaking onset and post-breaking period. A refined multiphase flow model has been employed to track the origin and trajectory for the jet and the splash-up using a multi-component PLIC-VOF approach together with Lagrangian particle tracking. First, the model is validated for a solitary wave propagating along a $s = 1/15$ slope, whereas the predicted breaking waves are compared both quantitatively and qualitatively with the detailed experimental measurements in terms of the wave breaking location, the shape of the plunging jet, and subsequent splash-up process. This provides us with the confidence to study the detailed wave breaking characteristics.

The mass transport under the shallow-water breaking waves is studied and the different regions in the interior of the wave can be tracked in an Eulerian way. The location and origin of the plunging jet can be clearly seen from the simulations. It is found that when the plunging jet impinges the undisturbed water surface ahead and splits into two parts: the front part of the jet moves upward with an angle to generate a secondary jet, which is comprised of the primary jet on the upper face and the undisturbed surface on the lower face; the rear part of the jet moves backward against the flow, creating a rough surface and circulation along the cavity. Two strong counter-rotating vortices can be observed during the splash-up process. The mass transport for

the splash-up process can be observed rather than from the conventional analysis of the velocity field.

In addition, Lagrangian particles are also seeded in the flow to track the particle trajectories. The interior particle trajectories and surface particle transport are shown and discussed, in comparison with its Eulerian counterpart. Compared to solitary waves on a flat bed, there is a backward motion for the particles in the vicinity of the plunging jet during the jet impingement. Both horizontal and vertical drift are analyzed and it is found that the maximum drifts are near the original location for the plunging jet while the total vertical drift is also high at the splash-up region. Furthermore, the detailed internal kinematics and dynamics of breaking waves are presented during wave overturning, impingement, and splash-up process, providing more detailed space-time resolution of the flow field to gain further insight into the plunging jet and splash-up in breaking waves.

The splash-up process depends on the wave breaking type. There is no splash-up when the wave breaks after the shoreline (such as collapsing and surging breakers) and also for the spilling breakers as the jet breaks into droplets and thin filament without generating the secondary jet. A secondary jet is observed for plunging breakers close to the shore, and jet-splash cycles are seen for plunging breakers further offshore. The air entrainment process in jet-splash cycles is different depending on the breaking strength.

Finally, the effect of the slope is investigated to quantify the difference between spilling, plunging, collapsing, and surging breaking waves. The surf-similar parameter in the literature is calculated, with a good agreement being obtained for different breakers.

The combined Eulerian and Lagrangian approach for breaking waves can help us better understand the pollutant and sediment transport process in the nearshore zone. Although only shallow-water breaking waves are considered here, the present model can also be applied for breaking waves in intermediate and deep water. Due to the restriction to analyze the geometric properties of the breaking waves, only 2D simulations are considered here. It is worth noting that actual breaking waves seen in nature are three-dimensional, in which the generation of turbulence and vortex structures are different from that observed in 2D simulations. The internal kinematics can be redistributed laterally during wave breaking, especially after jet impingement and splash-up process. In addition, the air entrainment under breaking waves is a 3D complex multiphase flow phenomenon involving bubbles and droplets, which have multiple length scales affected by the surface tension, turbulence, and mean flow. Future study will be

focused on the Lagrangian transport in 3D simulations, in which the energy dissipation mechanism and air entrainment are important.

AUTHOR DECLARATIONS

Conflict of Interest

The authors have no conflicts to disclose.

DATA AVAILABILITY

The data that support the findings of this study are available from the corresponding author upon reasonable request.

REFERENCES

[1] D. H. Peregrine, "Breaking waves on beaches," Annu. Rev. Fluid Mech. **15**, 149–178 (1983).

[2] M. Perlin, W. Choi, and Z. Tian, "Breaking waves in deep and intermediate waters," Annu. Rev. Fluid Mech. **45**, 115–145 (2013).

[3] P. L.-F. Liu, "Mass transport in water waves propagated over a permeable bed," Coastal Eng. **1**, 79–96 (1977).

[4] K. T. Kiger and J. H. Duncan, "Air-entrainment mechanisms in plunging jets and breaking waves," Annu. Rev. Fluid Mech. **44**, 563–596 (2012).

[5] F. Dias and J. M. Ghidaglia, "Slamming: Recent progress in the evaluation of impact pressures," Annu. Rev. Fluid Mech. **50**, 243–273 (2018).

[6] J. H. Duncan, "The breaking and non-breaking wave resistance of a two-dimensional hydrofoil," J. Fluid Mech. **126**, 507–520 (1983).

[7] J. C. Lin and D. Rockwell, "Evolution of a quasi-steady breaking wave," J. Fluid Mech. **302**, 29–44 (1995).

[8] R. J. Rapp and W. K. Melville, "Laboratory measurements of deep-water breaking waves," Philos. Trans. R. Soc. London, Ser. A **331**, 735–800 (1990).

[9] F. C. K. Ting and J. T. Kirby, "Observation of undertow and turbulence in a laboratory surf zone," Coastal Eng. **24**, 51–80 (1994).

[10] O. Kimmoun and H. Branger, "A particle image velocimetry investigation on laboratory surf-zone breaking waves over a sloping beach," J. Fluid Mech. **588**, 353–397 (2007).

[11] W. Wong, M. Bjørnestad, C. Lin, M. Kao, H. Kalisch, P. Guyenne, V. Roeber, and J. Yuan, "Internal flow properties in a capillary bore," Phys. Fluids **31**, 113602 (2019).

[12] Q. Wang, H. Liu, Y. Fang, and F. Dias, "Experimental study on free-surface deformation and forces on a finite submerged plate induced by a solitary wave," Phys. Fluids **32**, 086601 (2020).

[13] G. Antolloni, A. Jensen, J. Grue, B. Riise, and M. Brocchini, "Wave-induced vortex generation around a slender vertical cylinder," Phys. Fluids **32**, 042105 (2020).

[14] P. Bonmarin, "Geometric-properties of deep-water breaking waves," J. Fluid Mech. **209**, 405–433 (1989).

[15] D. R. Basco, "A qualitative description of wave breaking," J. Waterw. Port Coastal Ocean Eng. **111**, 171–188 (1985).

[16] P. Lin, *Numerical Modeling of Water Waves: An Introduction to Engineers and Scientists* (Taylor & Francis, 2008).

[17] G. Chen, C. Kharif, S. Zaleski, and J. Li, "Two-dimensional Navier–Stokes simulation of breaking waves," Phys. Fluids **11**, 121–133 (1999).

[18] P. Lubin, S. Vincent, S. Abadie, and J. P. Caltagirone, "Three-dimensional large eddy simulation of air entrainment under plunging breaking waves," Coastal Eng. **53**, 631–655 (2006).

[19] A. Iafrati, "Numerical study of the effects of the breaking intensity on wave breaking flows," J. Fluid Mech. **622**, 371–411 (2009).

[20] P. Lubin and S. Glockner, "Numerical simulations of three-dimensional plunging breaking waves: Generation and evolution of aerated vortex filaments," J. Fluid Mech. **767**, 364–393 (2015).

[21] L. Deike, W. K. Melville, and S. Popinet, "Air entrainment and bubble statistics in breaking waves," J. Fluid Mech. **801**, 91–129 (2016).

[22] Z. Wang, J. Yang, and F. Stern, "High-fidelity simulations of bubble, droplet and spray formation in breaking waves," J. Fluid Mech. **792**, 307–327 (2016).

[23] W. Chan, P. L. Johnson, P. Moin, and J. Urzay, "The turbulent bubble break-up cascade. Part 2. Numerical simulations of breaking waves," J. Fluid Mech. **912**, A43 (2021).

[24] P. Lin and P. L. F. Liu, "A numerical study of breaking waves in the surf zone," J. Fluid Mech. **359**, 239–264 (1998).

[25] P. Lin and P. L. F. Liu, "Turbulence transport, vorticity dynamics, and solute mixing under plunging breaking waves in surf zone," J. Geophys. Res.: Oceans **103**, 15677–15694, https://doi.org/10.1029/98JC01360 (1998).

[26] Y. Watanabe, H. Saeki, and R. J. Hosking, "Three-dimensional vortex structures under breaking waves," J. Fluid Mech. **545**, 291–328 (2005).

[27] E. D. Christensen, "Large eddy simulation of spilling and plunging breakers," Coastal Eng. **53**, 463–485 (2006).

[28] R. A. Dalrymple and B. D. Rogers, "Numerical modeling of water waves with the SPH method," Coastal Eng. **53**, 141–147 (2006).

[29] D. Lakehal and P. Liovic, "Turbulence structure and interaction with steep breaking waves," J. Fluid Mech. **674**, 522–577 (2011).

[30] Z. Xie, "Two-phase flow modelling of spilling and plunging breaking waves," Appl. Math. Modell. **37**, 3698–3713 (2013).

[31] B. Larsen and D. Fuhrman, "On the over-production of turbulence beneath surface waves in Reynolds-averaged Navier–Stokes models," J. Fluid Mech. **853**, 419–460 (2018).

[32] W. Mostert and L. Deike, "Inertial energy dissipation in shallow-water breaking waves," J. Fluid Mech. **890**, A12 (2020).

[33] M. Derakhti and J. T. Kirby, "Bubble entrainment and liquid–bubble interaction under unsteady breaking waves," J. Fluid Mech. **761**, 464–506 (2014).

[34] M. Derakhti and J. T. Kirby, "Breaking-onset, energy and momentum flux in unsteady focused wave packets," J. Fluid Mech. **790**, 553–581 (2016).

[35] Z. Xie, "A two-phase flow model for three-dimensional breaking waves over complex topography," Proc. R. Soc. A **471**, 20150101 (2015).

[36] Z. Xie and T. Stoesser, "Two-phase flow simulation of breaking solitary waves over surface-piercing and submerged conical structures," Ocean Eng. **213**, 107679 (2020).

[37] B. T. Paulsen, H. Bredmose, H. B. Bingham, and N. G. Jacobsen, "Forcing of a bottom-mounted circular cylinder by steep regular water waves at finite depth," J. Fluid Mech. **755**, 1–34 (2014).

[38] P. Lin, L. Cheng, and D. Liu, "A two-phase flow model for wave-structure interaction using a virtual boundary force method," Comput. Fluids **129**, 101–110 (2016).

[39] Z. Xie, T. Stoesser, S. Yan, Q. Ma, and P. Lin, "A Cartesian cut-cell based multiphase flow model for large-eddy simulation of three-dimensional wave-structure interaction," Comput. Fluids **213**, 104747 (2020).

[40] R. Scardovelli and S. Zaleski, "Direct numerical simulation of free-surface and interfacial flow," Annu. Rev. Fluid Mech. **31**, 567–603 (1999).

[41] F. H. Harlow and J. E. Welch, "Numerical calculation of time-dependent viscous incompressible flow of fluid with free surface," Phys. Fluids **8**, 2182–2189 (1965).

[42] C. W. Hirt and B. D. Nichols, "Volume of fluid (VOF) method for the dynamics of free boundaries," J. Comput. Phys. **39**, 201–225 (1981).

[43] S. J. Osher and J. A. Sethian, "Fronts propagating with curvature dependent speed: Algorithms based on Hamilton–Jacobi formulations," J. Comput. Phys. **79**, 12–49 (1988).

[44]S. O. Unverdi and G. Tryggvason, "A front-tracking method for viscous, incompressible, multi-fluid flows," J. Comput. Phys. **100**, 25–37 (1992).

[45]D. M. Anderson, G. B. McFadden, and A. A. Wheeler, "Diffuse-interface methods in fluid mechanics," Annu. Rev. Fluid Mech. **30**, 139–165 (1998).

[46]S. Koshizuka, A. Nobe, and Y. Oka, "Numerical analysis of breaking waves using the moving particle semi-implicit method," Int. J. Numer. Methods Fluids **26**, 751–769 (1998).

[47]X. Barthelemy, M. L. Banner, W. L. Peirson, F. Fedele, M. Allis, and F. Dias, "On a unified breaking onset threshold for gravity waves in deep and intermediate depth water," J. Fluid Mech. **841**, 463–488 (2018).

[48]M. Derakhti, J. T. Kirby, M. L. Banner, S. T. Grilli, and J. Thomson, "A unified breaking onset criterion for surface gravity waves in arbitrary depth," J. Geophys. Res.: Oceans **125**, e2019JC015886, https://doi.org/10.1029/2019JC015886 (2020).

[49]A. Varing, J. Filipot, S. Grilli, R. Duarte, V. Roeber, and M. Yates, "A new definition of the kinematic breaking onset criterion validated with solitary and quasi-regular waves in shallow water," Coastal Eng. **164**, 103755 (2021).

[50]Y. Li, "Tsunamis: Non-breaking and breaking solitary wave run-up," Ph.D. thesis (California Institute of Technology, 2000).

[51]S. T. Grilli, I. A. Svendsen, and R. Subramanya, "Breaking criterion and characteristics for solitary waves on slopes," J. Waterw. Port Coastal Ocean Eng. **123**, 102–112 (1997).

[52]P. Guyenne and S. T. Grilli, "Numerical study of three-dimensional overturning waves in shallow water," J. Fluid Mech. **547**, 361–388 (2006).

[53]C. Lachaume, B. Biausser, S. T. Grilli, P. Fraunie, and S. P. Guignard, "Modeling of breaking and post-breaking waves on slopes by coupling of BEM and VOF methods," in *Proceedings of the Thirteenth (2003) International Offshore and Polar Engineering Conference* (International Society of Offshore and Polar Engineers, 2003), Vol. 3, pp. 353–359.

[54]A. Khayyer, H. Gotoh, and S. D. Shao, "Corrected incompressible SPH method for accurate water-surface tracking in breaking waves," Coastal Eng. **55**, 236–250 (2008).

[55]B. Biausser, P. Fraunie, S. T. Grilli, and R. Marcer, "Numerical analysis of the internal kinematics and dynamics of 3-D breaking waves on slopes," Int. J. Offshore Polar Eng. **14**, 247–256 (2004); available at https://onepetro.org/IJOPE/article-abstract/28353/Numerical-Analysis-of-the-Internal-Kinematics-And.

[56]Z. Xie, "Numerical study of breaking waves by a two-phase flow model," Int. J. Numer. Methods Fluids **70**, 246–268 (2011).

[57]L. Deike, N. Pizzo, and W. K. Melville, "Lagrangian transport by breaking surface waves," J. Fluid Mech. **829**, 364–391 (2017).

[58]M. Paprota and W. Sulisz, "Particle trajectories and mass transport under mechanically generated nonlinear water waves," Phys. Fluids **30**, 102101 (2018).

[59]B. E. Launder and D. B. Spalding, "The numerical computation of turbulent flows," Comput. Methods Appl. Mech. Eng. **3**, 269–289 (1974).

[60]Z. Xie and T. Stoesser, "A three-dimensional Cartesian cut-cell/volume-of-fluid method for two-phase flows with moving bodies," J. Comput. Phys. **416**, 109536 (2020).

[61]Z. Xie, T. Stoesser, and J. Xia, "Simulation of three-dimensional free-surface dam-break flows over a cuboid, cylinder, and sphere," J. Hydraul. Eng. **147**, 06021009 (2021).

[62]Z. Xie, B. Lin, R. Falconer, S. Nichols, A. N. Tait, and K. Horoshenkov, "Large-eddy simulation of turbulent free surface flow over a gravel bed," J. Hydraul. Res. (published online 2022).

[63]O. Ubbink and R. I. Issa, "A method for capturing sharp fluid interfaces on arbitrary meshes," J. Comput. Phys. **153**, 26–50 (1999).

[64]D. Gueyffier, J. Li, A. Nadim, R. Scardovelli, and S. Zaleski, "Volume-of-fluid interface tracking with smoothed surface stress methods for three-dimensional flows," J. Comput. Phys. **152**, 423–456 (1999).

[65]J. Brackbill, D. Kothe, and C. Zemach, "A continuum method for modeling surface tension," J. Comput. Phys. **100**, 335–354 (1992).

[66]Z. Xie, D. Pavlidis, P. Salinas, C. C. Pain, and O. K. Matar, "A control volume finite element method for three-dimensional three-phase flows," Int. J. Numer. Methods Fluids **92**, 765–784 (2020).

[67]R. G. Dean and R. A. Dalrymple, *Water Wave Mechanics for Engineers and Scientists* (Prentice-Hall, Englewood Cliffs, NJ, 1984).

[68]G. G. Stokes, "On the theory of oscillatory waves," Trans. Cambridge Philos. Soc. **8**, 441–473 (1847).

[69]M. Longuet-Higgins, "Mass transport in water waves," Philos. Trans. R. Soc. London, Ser. A **245**, 535–581 (1953).

[70]K. A. Chang and P. L. F. Liu, "Velocity, acceleration and vorticity under a breaking wave," Phys. Fluids **10**, 327–329 (1998).

[71]A. L. New, "A class of elliptical free-surface flows," J. Fluid Mech. **130**, 219–239 (1983).